Flow around two elastically-mounted cylinders with different diameters in tandem and staggered configurations in the subcritical Reynolds number regime

Marek Jan Janocha [a,*], Muk Chen Ong [a], Per Richard Nyström [b], Zhenguo Tu [b], Geir Endal [c], Halvor Stokholm [c]

[a] *Department of Mechanical and Structural Engineering and Materials Science University of Stavanger, Stavanger, 4036, Norway*
[b] *IKM Ocean Design AS, Sandnes, 4313, Norway*
[c] *Equinor ASA, Fornebu, 1364, Norway*

A B S T R A C T

Flow around two cylinders with different diameters undergoing Flow-Induced Vibrations (FIV) in the subcritical flow regime is investigated using two-dimensional Unsteady Reynolds Averaged Navier-Stokes (URANS) approach. Physical parameters of the system are chosen to represent the free spanning pipelines laid in proximity. The two cylinders are initially placed at various tandem and staggered positions with one in the wake of the other, and subject to steady current flows. The two cylinders are free to respond in both in-line and transverse directions. The investigated Reynolds numbers (*Re*) are $Re_1 = 1.4 \times 10^5$ based on the diameter of the larger cylinder and $Re_2 = 1.15 \times 10^5$ based on the diameter of the smaller cylinder. A parametric study investigating the effects of relative spacing of the cylinders on the vibration response of the system is performed. First and second order statistics of the flow, frequency domain analysis and flow field visualizations are used to characterize the dynamic behavior of the system. It is found that the motion trajectories of the downstream cylinder show a qualitative difference depending upon whether it is in tandem with the upstream cylinder or in the wake with a transverse offset. A large amplification of the in-line response is observed in the positions with a transverse offset. The vibration response of the upstream cylinder is affected by the presence of the downstream cylinder only when the horizontal center-to-center distance is small ($L/D_1 = 2.06$ where D_1 is the diameter of the larger cylinder) and is largely unaffected when the horizontal distance is increased to $L/D_1 = 3.22$.

1. Introduction

Flow around tandem or staggered arrangements of elastically mounted cylinders is of practical engineering and academic interest and was studied extensively in the past. In the field of offshore engineering, relevant examples are marine riser arrays and subsea flowlines. In those applications, it is common to design clusters of long flexible cylinders running in parallel or nearly in parallel to each other. The riser interference problem is an important design driver for deep water floating installations. In practice, the importance of

---

(a) Close lay of two rigid pipelines at typical iceberg plough mark.

(b) Schematic diagram of pipelines routing over a complex topography.
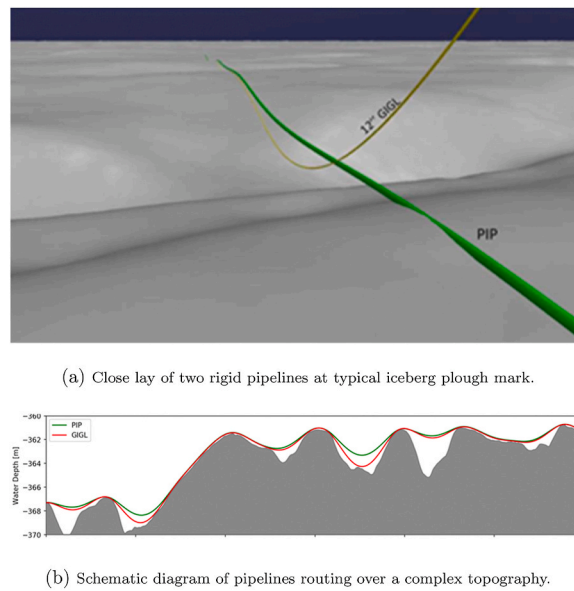
Fig. 1. Example of dual pipeline in close lay exposed to free spans [2].

the interaction effects is strongly influenced by the parameters of the system and detailed case specific analyses are recommended by the guidelines [1]. Another example where strong proximity interaction effects are expected is close lay of rigid flowlines. Lyngsaunet et al. [2] proposed a methodology of structural reliability assessment against trawl pull-over for two flowlines laid with a small separation distance. A significant cost optimization has been achieved by avoiding excessive seabed intervention works. However, the requirement of small separation distance may introduce additional challenges associated with complex hydrodynamics. In particular, when the subsea pipelines are laid in proximity and exposed to specific current directions, one of the cylinders can be positioned in the wake of the other. Furthermore, due to different engineering requirements (e.g. flow assurance, fatigue strength, over-trawl protection), different diameters of the flowlines are often encountered.

In many subsea projects, pipeline free spans are one of the major challenges [3]. Pipeline free spanning occurs when the contact between the pipeline and the seabed is not maintained over a certain distance. The pipeline free span scenario can be permanent, when generated by seabed roughness, or characterized by time evolution due to seabed mobility and scouring processes [3]. The consequence of the free span formation is development of the gap between the seabed and the pipeline surface. A typical dual pipeline free span situation, as discussed by Lyngsaunet et al. [2], is depicted in Fig. 1. The hydrodynamics around a cylinder close to a plane boundary is considerably different from that of a cylinder placed at a distance from a plane boundary. It has been shown that the plane boundary presence inhibits the vortex shedding from a cylinder if the gap ratio (e/D where e is the distance between the bottom surface of the cylinder and the wall, D is the diameter of the cylinder) is smaller than 0.3 for a fixed cylinder [4] and $e/D < 0.05$ for an elastically supported cylinder [5]. Vortex shedding from the cylinder surface results in periodically oscillating drag and lift force components acting on the cylinder. If the cylinder is elastically supported, these forces may induce structural vibrations. The synchronization between the vortex shedding frequency and the natural frequency of the structure may cause large-amplitude oscillations leading to fatigue damage or structural failure. More details about the vortex-induced vibrations (VIV) can be found in the comprehensive reviews by Williamson & Govardhan [6], Sarpkaya [7], Gabbai & Benaroya [8] and Bearman [9].

The hydrodynamics around two cylinders in proximity is further complicated. A comprehensive review of the influence of the configuration on the flow was carried out by Zdravkovich [10] and updated based on more recent advances in the field by Sumner [11]. The most widely adopted classification of the interaction regions for two cylinders configurations was proposed by Zdravkovich [12,13] and Medeiros & Zdravkovich [14]. Four main regions can be distinguished, i.e., the proximity interference region, the proximity and wake interference region, the wake interference region, and no interference region. In the proximity interference region, two cylinders are placed close to each other in a side-by-side configuration or at a high angle α defined as the angle between the freestream flow direction and the line connecting the centers of the cylinders. Characteristic coupled vortex shedding occurs in this region resulting in the formation of a single vortex street. Considering two cylinders with identical diameters in tandem arrangement the relative position of the cylinders can be defined as a non-dimensional spacing ratio (L/D) where L is the center-to-center distance between the two cylinders. For tandem arrangements and slightly staggered arrangements ($\alpha < 10°$) the proximity and wake interference region occurs at $1 < L/D < 4$ and transitions into the wake interference region after exceeding critical value of the spacing ratio, $L/D > 4$. In those regions, the downstream cylinder is strongly affected by the wake of the upstream cylinder. The upstream cylinder is affected by the feedback mechanism for L/D values up to 8, as demonstrated by Alam et al. [15,16]. However, the feedback effects are decaying rapidly after exceeding spacing of $L/D = 4$.

Very few systematic studies focused on VIV of two cylinders in proximity have been undertaken in the past ([17], [18], [19] [20]). King & Jones [19] conducted experiments in water with two flexible cylinders at $Re = 1 \times 10^3 - 29 \times 10^3$ ($Re = U_\infty D/\nu$ where U_∞ is

the free stream flow velocity and ν is the kinematic viscosity of the fluid). The horizontal separation was in the range of $L/D = 0.25 - 6.0$. They observed that the upstream cylinder behaves like an isolated cylinder undergoing VIV. The response of the downstream cylinder demonstrated a similar build-up of oscillation amplitudes to that of the upstream cylinder. However, with increasing reduced velocities ($U_r = U_\infty/f_nD$ where f_n is the natural frequency in still water), the oscillations remained at a high level, contrary to the upstream cylinder response which showed a typical reduction of oscillation after leaving synchronization range. Assi et al. [21] investigated a mechanism of wake-induced vibration (WIV) by performing a series of experiments with two tandem cylinders in a recirculating water channel. They demonstrated that the wake-displacement mechanism proposed by Zdravkovich [17] is the correct explanation of the wake-induced vibration phenomenon. According to Assi et al. [21] the WIV mechanism is sustained by the energy input from the unsteady vortex-structure interaction experienced by the downstream cylinder. By performing an additional experiment with a simulated sheared flow in place of an upstream cylinder, they verified that WIV is not a resonant phenomenon.

More recently, Computational Fluid Dynamics (CFD) methods have increasingly been applied in the field of marine hydrodynamics. The applicability of Unsteady Reynolds-averaged Navier-Stokes (URANS) approach to simulate the flow mechanism around the marine pipeline close to a plane wall was investigated by Ong et al. [22]. Standard $k - \varepsilon$ model was used in their study for simulations in the subcritical and supercritical flow regimes. Ong et al. [22] reported satisfactory agreement with published experimental data. Han et al. [23] and Kang et al. [24] performed two-dimensional URANS simulations of a single cylinder VIV in the subcritical flow regime using a $k - \omega$ SST model. Studies by Han et al. [23] and Kang et al. [24] successfully reproduced the branching behavior reported by Jauvtis & Williamson [25] confirming the ability of 2D URANS simulations to predict the response amplitudes and frequencies of VIV in the subcritical regime with reasonable accuracy. As pointed out by Kinaci [26], the URANS simulations can provide accurate and fast results quantitatively for practical engineering purposes. Therefore, this approach is applicable in the frame of parametric studies where a large number of cases is considered and low computational cost and time are essential.

In the present study, flow around two elastically mounted cylinders with different diameters in tandem and staggered arrangements undergoing 2DOF vibrations is investigated numerically. Multiple horizontal and vertical spacings are studied, and their influence on the vibration amplitudes and frequencies is analyzed. The Reynolds numbers are $Re_1 = 1.4 \times 10^5$ based on the diameter of the larger cylinder and $Re_2 = 1.15 \times 10^5$ based on the diameter of the smaller cylinder.

The rest of the paper is organized as follows. In Section 2, the mathematical formulation and the numerical model used in the present study are outlined. Description of the computational domain and sensitivity studies on grid density and time step size are provided. The present numerical model is compared with the results from other similar published studies. In Section 3, the results of numerical simulations performed with different positions of the downstream cylinder at two different current velocities are presented. Finally, conclusions are given in Section 4.

2. Mathematical formulation

2.1. Flow model

The governing equations for the fluid flow considered in the present study are the two-dimensional incompressible Reynolds-averaged Navier-Stokes equations. The equations of continuity and momentum conservation are given by:

$$\frac{\partial u_i}{\partial x_i} = 0 \tag{1}$$

$$\frac{\partial u_i}{\partial t} + u_j \frac{\partial u_i}{\partial x_j} = -\frac{1}{\rho} \frac{\partial p}{\partial x_i} + \frac{\partial}{\partial x_j} \left[(\nu + \nu_t) \left(\frac{\partial u_i}{\partial x_j} + \frac{\partial u_j}{\partial x_i} \right) \right] \tag{2}$$

where $i, j = 1, 2$; x_1, x_2 are streamwise and wall-normal directions, respectively; u_1, u_2 are the averaged flow velocity components corresponding to directions x_1 and x_2; ν denotes the kinematic viscosity of the fluid; ν_t is the eddy viscosity, ρ is the density of the fluid; p is the dynamic pressure. The shear stress transport (SST) $k - \omega$ turbulence model [27] is used in the present study to calculate eddy viscosity by solving the two variables, namely, the turbulent kinetic energy (k) and the specific turbulent dissipation rate (ω). Transport equations for specific dissipation rate ω and turbulent kinetic energy k are given by:

$$\frac{D(\rho k)}{Dt} = \tilde{P}_k - \beta^* \rho k \omega + \frac{\partial}{\partial x_j} \left[(\mu + \sigma_k \mu_t) \frac{\partial k}{\partial x_j} \right] \tag{3}$$

$$\frac{D(\rho \omega)}{Dt} = \alpha \rho S^2 - \beta \rho \omega^2 + \frac{\partial}{\partial x_j} \left[(\mu + \sigma_\omega \mu_t) \frac{\partial \omega}{\partial x_j} \right] + 2(1 - F_1)\rho \frac{\sigma_{\omega 2}}{\omega} \frac{\partial k}{\partial x_j} \frac{\partial \omega}{\partial x_j} \tag{4}$$

where $\tilde{P}_k$ is a production limiter term given by the equation:

$$\tilde{P}_k = \min \left[\mu_t \frac{\partial u_i}{\partial x_j} \left(\frac{\partial u_i}{\partial x_j} + \frac{\partial u_j}{\partial x_i} \right), 10\beta^* \rho k \omega \right] \tag{5}$$

Variable φ_1 denotes any constant in the standard $k - \omega$ model and variable φ_2 denotes any constant in the standard $k - \varepsilon$ model. The blending function F_1 is used to calculate the corresponding constant of the $k - \omega$ SST model from Eq. (3) and Eq. (4) by:
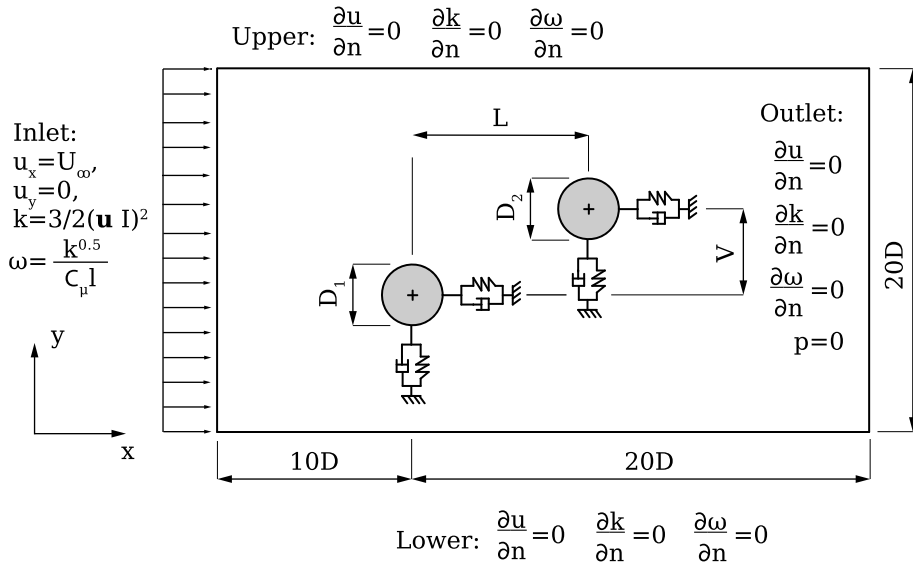
Fig. 2. Schematic diagram of the computational domain and imposed boundary conditions.

$$\varphi = F_1\varphi_1 + (1 - F_1)\varphi_2 \tag{6}$$

$$F_1 = \tanh\left[\left[\min\left[\max\left(\frac{\sqrt{k}}{\beta^*\omega y}, \frac{500\nu}{y^2\omega}\right), \frac{4\rho\sigma_{\omega 2}k}{CD_{k\omega}y^2}\right]\right]^4\right] \tag{7}$$

$$CD_{k\omega} = \max\left[2\rho\frac{\sigma_{\omega 2}}{\omega}\frac{\partial k}{\partial x_j}\frac{\partial \omega}{\partial x_j}, 10^{-10}\right] \tag{8}$$

where y is the distance to the nearest wall, $CD_{k\omega}$ is the positive part of the cross-diffusion term in Eq. (4), and the turbulent eddy viscosity ν_t is defined as:

$$\nu_t = \frac{a_1 k}{\max(a_1\omega, SF_2)} \tag{9}$$

where S is the strain rate invariant and F_2 is a second blending function given by:

$$F_2 = \tanh\left[\left[\max\left(\frac{2\sqrt{k}}{\beta^*\omega y}, \frac{500\nu}{y^2\omega}\right)\right]^2\right] \tag{10}$$

Model constants: σ_k, σ_ω, β, β^*, γ take standard values as defined in Ref. [27].

2.2. Structural model

In the present study, we consider two elastically supported cylinders experiencing VIV as shown in Fig. 2. The flow direction is from left to right of the domain. The dynamic behavior of the cylinders vibrating with 2DOF is modeled as a mass-spring-damper system. The equations of motion of cylindrical structure are as follows:

$$m\frac{\partial^2 x}{\partial t^2} + c\frac{\partial x}{\partial t} + k_{s,x}x = F_x(t) \tag{11}$$

$$m\frac{\partial^2 y}{\partial t^2} + c\frac{\partial y}{\partial t} + k_{s,y}y = F_y(t) \tag{12}$$

where x and y denote the in-line and transverse displacements respectively; $k_{s,x}$ and $k_{s,y}$ is the structural stiffness in the in-line and transverse directions respectively; c is the structural damping; m is the structural mass; F_x and F_y are the fluid forces acting in the in-line and transverse directions, respectively. The mass ratio m^* and damping coefficient ζ are expressed as:

$$m^* = \frac{m}{m_d}, \quad \zeta = \frac{c}{2\sqrt{k_s m}}, \tag{13}$$

where m is the mass of the cylinder, m_d is the mass of displaced fluid. The reduced velocity, U_r is defined as $U_r = U_\infty / (f_{n,y} D)$, where $f_{n,y}$ is the transverse structural natural frequency in still water, U_∞ is the free stream flow velocity. C_D and C_L are the drag and lift coefficients, respectively, computed by:

$$C_D = \frac{F_x}{\frac{1}{2} U_\infty^2 \rho D L_z} \tag{14}$$

$$C_L = \frac{F_y}{\frac{1}{2} U_\infty^2 \rho D L_z} \tag{15}$$

where ρ is the fluid density and L_z represents span-wise dimension of the cylinder. The fluid forces F_x and F_y are obtained by solving the flow equations Eq. (1) and Eq. (2) coupled with the structural equations Eq. (11) and Eq. (12). The temporal integration of the dynamic equations is performed numerically using the Newmark - β algorithm.

2.3. Numerical solution procedure, computational domain and boundary conditions

Simulations are performed using the open source CFD toolbox OpenFOAM. Pressure-velocity coupling is solved using PIMPLE algorithm combining Semi-Implicit Method for Pressure Linked Equations (SIMPLE) and Pressure Implicit with Split Operators (PISO) methods. The implicit second-order Crank-Nicolson scheme is used for the time integration. The divergence and gradient terms are discretized using Gauss linear integration scheme. The Laplacian and surface normal gradients are discretized using Gauss linear integration with limited non-orthogonal correction. All the employed schemes are of second-order accuracy.

A schematic of the investigated problem consisting of flow around two vibrating cylinders with different diameters is presented in Fig. 2. In the present study, a rectangular computational domain is established with dimensions of $30D_1$ by $20D_1$. Here D_1 is the diameter of the larger cylinder and D_2 is the diameter of the smaller cylinder. The upstream cylinder (UC) center is located at a distance $10D_1$ from the inflow and $20D_1$ from the outflow. The downstream cylinder (DC) center is located at vertical center-to-center offset V and horizontal center-to-center offset L. The upper and lower boundaries are located at a distance $10D_1$ from the larger cylinder center. These domain settings result in a blockage ratio of 5% which is considered sufficient to minimize the numerical error associated with the proximity of the boundary conditions imposed at the upper and lower sides of the domain and at the outlet.

1. Uniform inlet flow profile is specified as follows:

$$u_1 = U_\infty \tag{16}$$

$$u_2 = 0 \tag{17}$$

$$k = \frac{3}{2} (\boldsymbol{u} I)^2 \tag{18}$$

$$\omega(y) = \frac{\sqrt{k}}{C_\mu \ell} \tag{19}$$

where $C_\mu = 0.09$ is the model constant; $I = 0.9\%$ is the turbulent intensity; ℓ is the turbulent length scale.

2. At the outlet of the domain u, k and ω are prescribed with zero normal gradient condition, the reference pressure is set $p = 0$.
3. At the top boundary u, k, ω and p are set to zero normal gradient.
4. On the cylinder walls a 'no-slip' condition is imposed: $u_1 = 0$, $u_2 = 0$, $k = 0$, and $\omega = \frac{60\nu}{\beta_1 (h_p)^2}$ where $\beta_1 = 0.075$ is the model constant, h_p is the radial distance from the wall to the first adjacent cell center in computational grid. The $k - \omega$ SST model is used with a fine near-wall mesh $y^+ < 1$. A non-dimensional wall distance is defined here as:

$$y^+ = \frac{u_* h_p}{\nu} \tag{20}$$

where ν is the kinematic viscosity of the fluid and u_* is the friction velocity.

Friction velocity is defined as:

$$u_* = \sqrt{\frac{\tau_w}{\rho}} \tag{21}$$

where τ_w is the wall shear stress. The movement of the boundaries of cylinders is realized using a dynamic mesh method.

2.4. Input parameters

A summary of parameters used in the simulations is presented in Table 1. Parameters are selected to approximate a real case of a

Table 1
Parameters of the structures investigated in the present study.

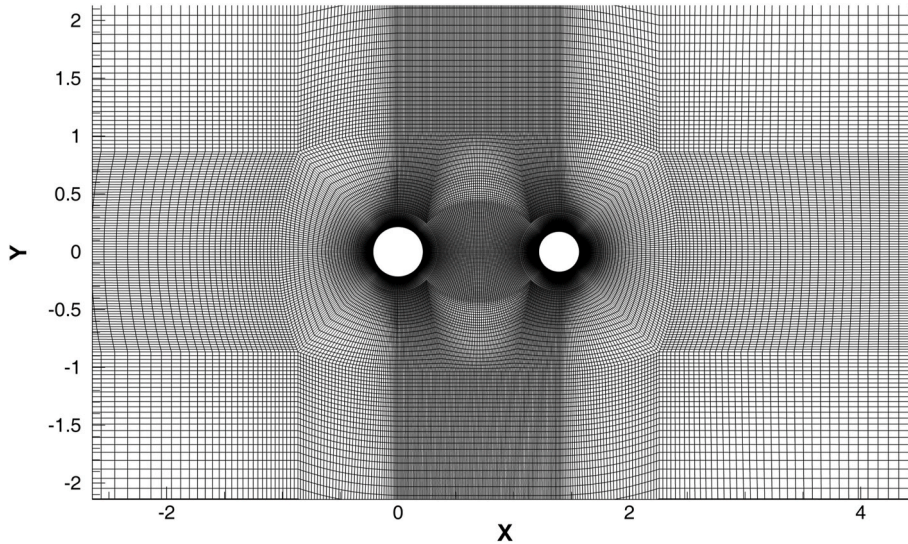| Parameter	Upstream cylinder	Downstream cylinder
Mass ratio m^*	2.20	1.56
Diameter D_n	0.433 m	0.350 m
In-line natural frequency $f_{n,x}$	0.183 Hz	0.142 Hz
Cross-flow natural frequency $f_{n,y}$	0.462 Hz	0.356 Hz
Damping ratio ζ	1.5%	1.5%
Reynolds number Re	1.4×10^5	1.15×10^5
Reduced velocity $U_r = \dfrac{U_\infty}{f_{n,y} D_n}$	2.5	4

Fig. 3. Example of a computational grid for flow around a tandem cylinders vibrating with 2DOF (87 024 elements, $L/D_1 = 3.22$, $V/D_1 = 0$).

Table 2
Near-wall grid refinement sensitivity study results.

Grid parameters:		Hydrodynamic parameters:						
Case								
layer height h_p	$\overline{C}_{D,1}$	$C_{L,1}^{rms}$	$y_{max,1}^+$	$y_{avg,1}^+$	$\overline{C}_{D,2}$	$C_{L,2}^{rms}$	$y_{max,2}^+$	$y_{avg,2}^+$
M3A	$0.001\ D_1$	0.8227	0.7469	7.866	4.126	0.3938	1.2605	6.362	4.307
M3B	$0.0005\ D_1$	1.0632	1.0111	3.986	2.069	0.5322	1.7530	3.377	2.205
M3C	$0.0002\ D_1$	1.0490	1.0201	1.521	0.841	0.5270	1.7486	1.292	0.900
M3D	$0.0001\ D_1$	1.0431	1.0041	0.742	0.418	0.5227	1.6569	0.628	0.447

midspan cross-section of two pipelines exposed to a large free span and uniform current. The natural frequencies in the transverse and in-line directions are fundamental mode frequencies calculated using a finite element model of the free spanning pipelines.

2.5. Convergence studies

The grid density and time step sensitivity studies are performed for the two cylinders configuration with a vertical offset $V/D_1 = 0$ and a horizontal offset $L/D_1 = 3.22$. The cylinders are free to vibrate in both x and y directions. The spatial domain is discretized with a block structured grid composed of hexahedral cells. Fig. 3 shows a typical computational grid used in the present study. The grid is refined in the areas of the domain where sharp local gradients of flow variables are expected and close to the walls. The near-wall grid expansion ratio (r_e) is kept smaller than 1.05 for the first 20 cell layers and is approximately $r_e = 1.2$ in the remaining part of the domain. In the first step, the influence of the near wall grid refinement is investigated in order to ensure a sufficient grid resolution to resolve the viscous sublayer. Parameter varied in the study is the first cell layer height near the cylinders surfaces. The Reynolds

Table 3
Grid density sensitivity study results.

Grid parameters:		Hydrodynamic parameters:					
Case	Elements	$\overline{C}_{D,1}$	$C_{L,1}^{rms}$	St_1	$\overline{C}_{D,2}$	$C_{L,2}^{rms}$	St_2
M1C	23 000	0.9694	0.7718	0.301	0.4076	1.1883	0.244
M2C	34 844	1.0206	0.9038	0.306	0.4653	1.4779	0.247
M3C	55 068	1.0490	1.0201	0.304	0.5270	1.7486	0.245
M4C	87 024	1.0890	1.0458	0.304	0.5448	1.6662	0.245
M5C	126 260	1.0987	1.0885	0.303	0.5526	1.6966	0.245
M6C	183 060	1.1012	1.0863	0.303	0.5604	1.7263	0.245

Table 4
Time step sensitivity study results.

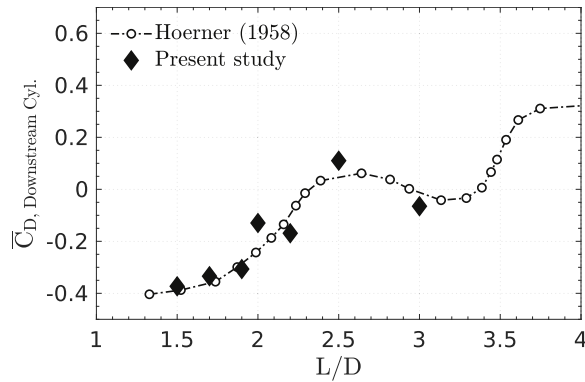| Grid parameters:			Hydrodynamic parameters:					
Case	Time step	Elements	$\overline{C}_{D,1}$	$C_{L,1}^{rms}$	St_1	$\overline{C}_{D,2}$	$C_{L,2}^{rms}$	St_2
M4CT1	$\Delta t = 0.008$	87 024	1.0850	1.0442	0.304	0.5431	1.6091	0.245
M4CT2	$\Delta t = 0.004$	87 024	1.0831	1.0458	0.304	0.5401	1.6662	0.245
M4CT3	$\Delta t = 0.002$	87 024	1.0802	1.0428	0.304	0.5409	1.6455	0.245

Fig. 4. Comparison of mean drag coefficient of downstream cylinder predicted by the present model with the experimental data.

Table 5
Summary of physical properties used in the simulations of an isolated cylinder vibrating with 2DOF.

Parameter	Value
Cylinder diameter D [m]	0.0635
Cylinder mass per unit length [kg/m]	17.1
Added mass per unit length [kg/m]	3.16
Fluid density [kg/m^3]	1000
Mass ratio m^* [−]	5.4
Damping factor ζ [−]	0.002
Natural frequency in still water [Hz]	1.18
Turbulent intensity I [%]	1

number based on the free stream velocity U_∞, diameters of the cylinders D_1, D_2 and the kinematic viscosity ν is kept constant at $Re_1 = 1.4 \times 10^5$ and $Re_2 = 1.15 \times 10^5$ for the upstream and downstream cylinders, respectively. The Courant number defined as $Co = \frac{u\Delta t}{\Delta x}$ is kept smaller than 0.8 during the simulations. A summary of the simulations parameters and obtained hydrodynamic quantities is shown in Table 2. Maximum and average values of y^+ are calculated on respective cylinders walls based on u_* extracted from the simulations. In the case of first cell layer height $h_p = 0.001D_1$, a significant deviation of the obtained results is observed compared to the other investigated cases. In the remaining cases, the solution is not sensitive to further decrease of h_p. In the remaining simulations,
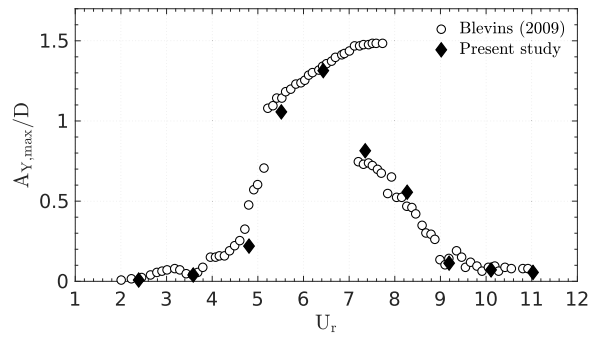
Fig. 5. Comparison of response amplitudes in transverse direction with experimental data.
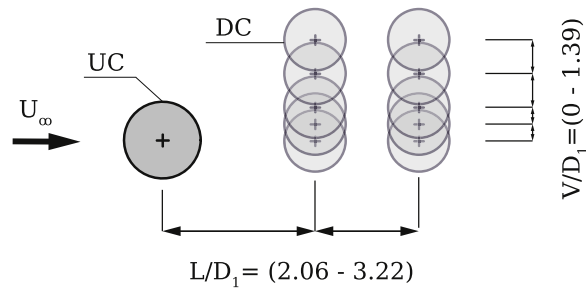

Fig. 6. Schematic of cylinders configurations simulated in the present study.
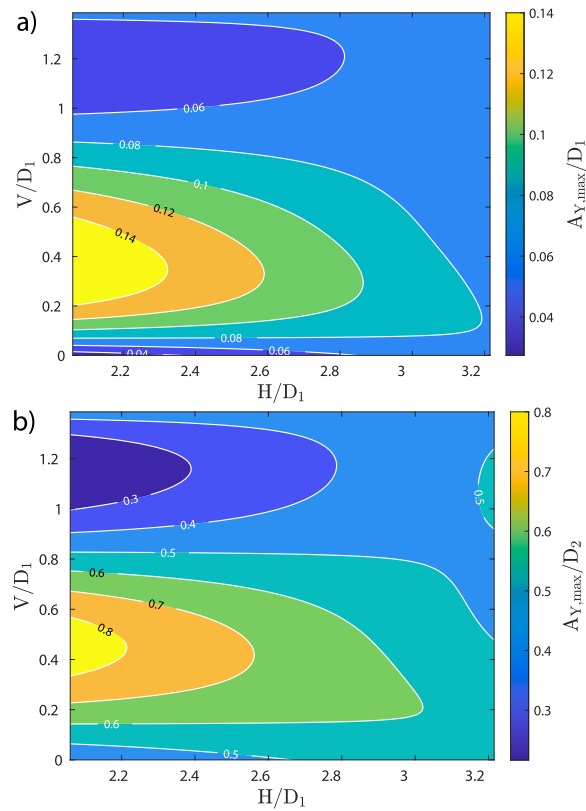

Fig. 7. Variations of the normalized transverse amplitude response for different horizontal and vertical offsets. Upstream cylinder (a) and downstream cylinder (b).
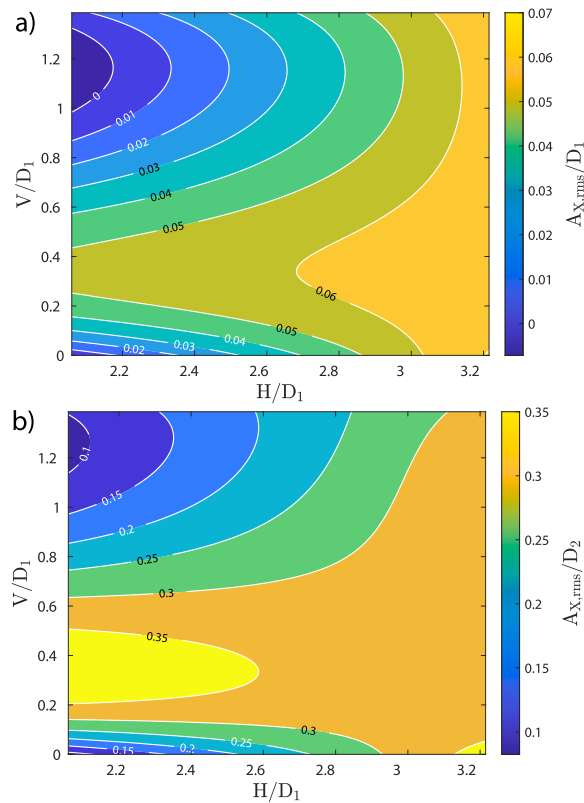
Fig. 8. Variations of the normalized in-line amplitude response for different horizontal and vertical offsets. Upstream cylinder (a) and downstream cylinder (b).

$h_p = 0.0002D_1$ is selected ensuring that average y^+ value is smaller than one.

The grid density sensitivity study is performed on five computational grids with different cell densities generated using a constant refinement factor $r_F = 1.25$. The geometric similarity of all generated grids is preserved. The time step (Δt) used in the grid density sensitivity study is restricted by a maximum $Co < 0.8$ and Δt is adjusted automatically by the solver accordingly. Results of the grid sensitivity study are presented in Table 3. It can be concluded that for the computational grids with density higher than approximately 90.000 cells, a further grid refinement shows negligible influence on the compared hydrodynamic quantities.

In order to evaluate the effect of Δt size, three fixed Δt settings are tested on the computational grid from the case M4C (with $\Delta t = 0.004$, average $Co \approx 0.5$ on grid M4C). A summary of Δt sensitivity study is given in Table 4. It appears that the solutions of the present simulations are relatively insensitive to Δt size in the range between 0.002 and 0.008. In the remaining simulations, adjustable Δt restricted by maximum $Co < 0.8$ criterion is used to ensure the solution accuracy and capture transient effects of the modeled physical phenomena.

Based on the sensitivity studies results, it appears that the grid with 87 024 elements and time step restricted by maximum $Co < 0.8$ provide acceptable spatial and temporal resolution for the simulation of flow-induced vibrations of two cylinders in the subcritical Reynolds number regime. This is supportive for the selection of grid type M4C, providing a good balance of computational cost and accuracy. Grids used in the validation studies and in the main parametric study have similar density and topology to that of the grid M4C.

2.6. Model validation studies

The present model is used to simulate the flow around a stationary tandem cylinders with equal diameters. The calculated hydrodynamic forces are compared with the experimental data from Hoerner [28]. The domain size and boundary conditions are the same as shown in Fig. 2. Fig. 4 shows the mean drag coefficient of the downstream cylinder obtained from the simulations of two tandem cylinders at $Re = 10^4$ subject to a uniform current. Overall, a good agreement with the experimental data is reported and the present simulations can predict the drag force reduction on the downstream cylinder due to the interaction with the wake of the upstream cylinder.

The model ability to predict the vortex-induced vibration amplitudes and frequencies is validated by performing a set of simulations of an isolated cylinder vibrating with 2DOF at selected U_r in range $3 \leq U_r \leq 13$. The validation study is set up according to the experiment settings reported by Blevins & Coughran [29] which are summarized in Table 5. Fig. 5 shows the normalized maximum
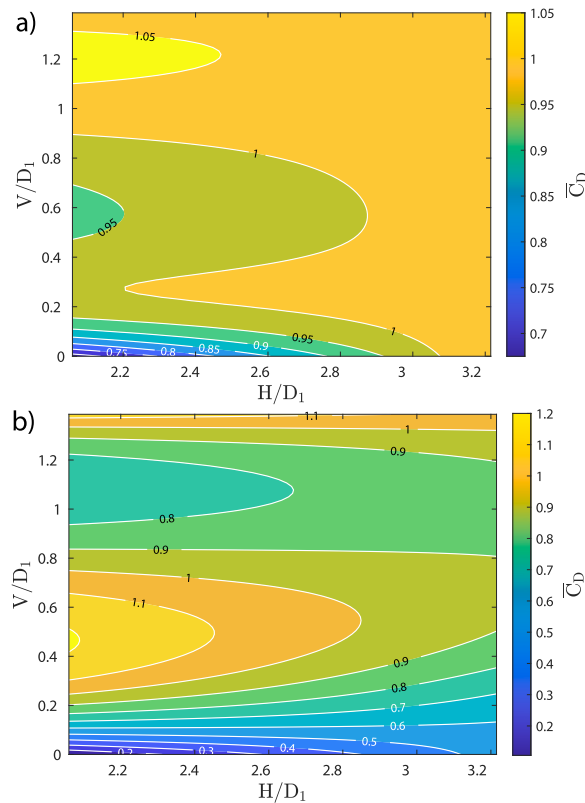
Fig. 9. Variations of the mean drag coefficient for different horizontal and vertical offsets. Upstream cylinder (a) and downstream cylinder (b).

transverse vibration amplitudes ($A_{Y,max}/D$) versus U_r predicted by the present numerical model compared to the experimental data. As the natural frequency of the cylinder approaches the vortex shedding frequency, the lock-in phenomenon is observed in which the response amplitude of the cylinder is increased significantly. The present model appears to predict the onset of the lock-in with reasonable accuracy. The branching behavior described by Jauvtis & Williamson [25] is clearly visible in Fig. 5 with three distinguishable branches, namely the initial branch, the upper branch, and the lower branch. The peak response in the super upper branch is known to exhibit a hysteretic behavior. The predicted $A_{Y,max}/D$ around $U_r = 7$ are close to the measured $A_{Y,max}/D$ for the lower branch. The high $A_{Y,max}/D$ values in the upper branch are not observed. This can be attributed to the fact that present simulations are carried out at fixed flow velocities. As discussed by Han et al. [23] and Kang et al. [24], in order to reach the highest $A_{Y,max}/D$ values in the upper branch, a gradual increase of the flow velocity is required. Generally, the present approach seems to provide reasonable accuracy and performance in capturing the essential physics of flow-induced vibrations.

Following a series of convergence and validation studies, the results obtained from the CFD simulations are supporting the validity of the present model to predict the flow physics and fluid-structure-interaction between two circular cylinders in close proximity with acceptable accuracy. Computational grids used in the remaining part of the study are of similar density to the grid M4C (approximately 87 000 cells) with a near wall cell distribution assuring at least 15 cell layers in the viscous sub-layer and time-step adjusted dynamically, limited by the maximum $Co < 0.8$.

3. Results and discussion

The case matrix established in the present study is visualized in Fig. 6. The effects of configuration on the dynamic behavior of two cylinders are investigated over the ranges of horizontal offset $L/D_1 = [2.06, 3.22]$ and vertical offset $V/D_1 = [0, 0.23, 0.46, 0.92, 1.39]$. For each simulated case, the computation is performed for 500 units of non-dimensional time ($\tau = tU_\infty/D_1$). The structural and flow parameters used in the simulations are summarized in Table 1 and are the same as those used in the sensitivity studies.

3.1. Effect of spacing on the amplitude and force responses

The maximum transverse vibration amplitudes ($A_{Y,max}/D_n$) are normalized by the diameter of respective cylinders where subscript $n = 1$ denotes UC and $n = 2$ denotes DC. $A_{Y,max}/D_n$ versus L/D_1 and V/D_1 is shown in the contour maps for UC (Fig. 7a) and DC (Fig. 7b), respectively. From the contours of $A_{Y,max}/D_n$, it is evident that proximity effects are significant for both UC and DC responses at $L/D_1 = 2.06$ and decay rapidly with an increase in the horizontal offset indicated by a much smaller variability at $L/D_1 = 3.22$. The
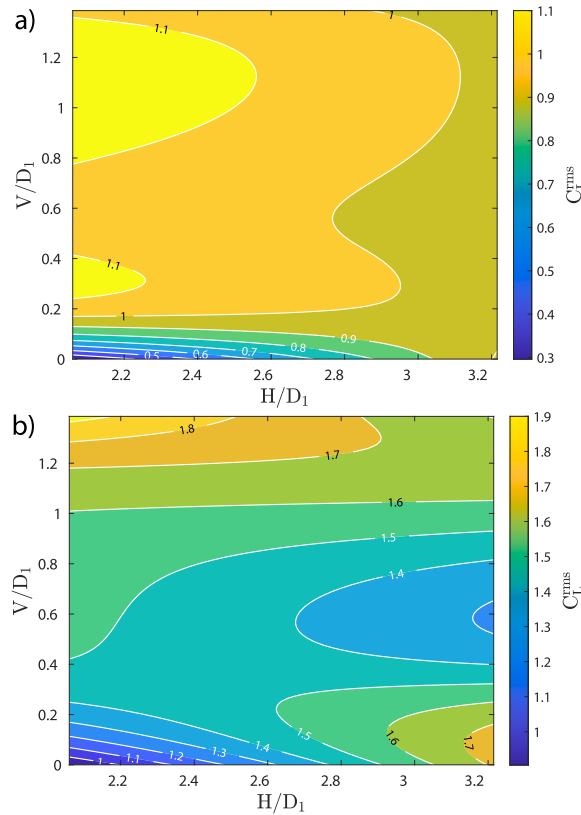
Fig. 10. Variations of the root-mean-square lift coefficient for different horizontal and vertical offsets. Upstream cylinder (a) and downstream cylinder (b).

reduced velocity $U_r = 2.5$ experienced by UC corresponds to the pre-lock-in regime and is characterized by small amplitudes of transverse vibration. DC is experiencing large vibration amplitudes and U_r is equal to 4 which is typically associated with the onset of VIV lock-in. Based on the effect of V/D_1 on $A_{Y,max}/D_n$, three distinct zones can be distinguished: (i) low-response zone close to UC centerline, (ii) high-response zone at intermediate vertical offsets ($V/D_1 = 0.2 - 0.6$), and (iii) low-response zone at large vertical offsets ($V/D_1 > 0.6$). The peak response in $A_{Y,max}/D_n$ is observed for the ($L/D_1 = 2.06$, $V/D_1 = 0.46$) configuration. When L/D_1 is increased from 2.06 to 3.22, $A_{Y,max}/D_n$ is considerably less sensitive to change in V/D_1.

The normalized root-mean-square in-line vibration amplitude ($A_{X,rms}/D_n$) is presented in Fig. 8. $A_{X,rms}/D_1$ is relatively small and increases with an increase in L/D_1, as evidenced in Fig. 8a. The $A_{X,rms}/D_2$ values presented in Fig. 8b are characterized by response zones which generally overlap with those identified for the $A_{Y,max}/D_2$ response (Fig. 7b). When the cylinders are located close to each other ($L/D_1 = 2.06$) the effect of V/D_1 on $A_{X,rms}/D_n$ is very strong. The jump in $A_{X,rms}/D_2$ response occurs analogically to the jump in $A_{Y,max}/D_2$ response. Peak in-line response is observed for the ($L/D_1 = 2.06$, $V/D_1 = 0.46$) configuration. In the high response zone $A_{X,rms}/D_2$ is increased significantly compared to the isolated cylinder case, where a typical in-line amplitude is approximately one order of magnitude lower than the corresponding transverse amplitude [25]. Another feature which can be observed in the $A_{X,rms}/D_2$ response is the enhanced in-line vibration of DC for $L/D_1 = 3.22$. This indicates that for larger L/D_1 even at higher V/D_1, DC is interacting with the wake of UC. The increase $A_{X,rms}/D_2$ is primarily the effect of wake-induced vibrations.

Mean hydrodynamic coefficients are calculated after the flow reaches a steady state. The effect of spacing on the mean drag co-efficient ($\overline{C}_D$) is visualized on the contour plots shown in Fig. 9. The drag reduction due to the shielding effect [30] is very apparent in Fig. 9b for tandem cylinders configurations ($L/D1 = 2.06$, $V/D1 = 0$ and $L/D1 = 3.22$, $V/D1 = 0$). For ($L/D1 = 2.06$, $V/D1 = 0$) configuration $\overline{C}_D$ of DC is close to zero. The shielding effect decays with an increase in $V/D1$. Due to the wake widening for larger $L/D1$ the shielding effect is present also for small $V/D1$. The $\overline{C}_D$ of UC is also reduced but the drag reduction effect is much smaller compared to that observed for DC and occurs only when L/D_1 is sufficiently small (i.e. $L/D_1 = 2.06$). A slight increase in the $\overline{C}_D$ value of DC is observed in the ($L/D1 = 2.06$, $V/D1 = 0.46$) configuration where the peak vibration amplitudes are observed.

The effect of spacing on the root-mean-square lift coefficient ($C_{L,rms}$) is presented in Fig. 10. The $C_{L,rms}$ value of UC is largely un-affected by the presence of DC with the exception of ($L/D_1 = 2.06$, $V/D_1 = 0$) configuration, where a considerable reduction of $C_{L,rms}$ is observed. However, DC shows large sensitivity of $C_{L,rms}$ with respect to spacing. Similarly to the drag force reduction, $C_{L,rms}$ is reduced when DC is located in the wake of UC. The effect is the strongest for the ($V/D_1 = 0$, $L/D_1 = 2.06$) configuration. When L/D_1 is extended to 3.22, the $C_{L,rms}$ values are similar for all investigated V/D_1.
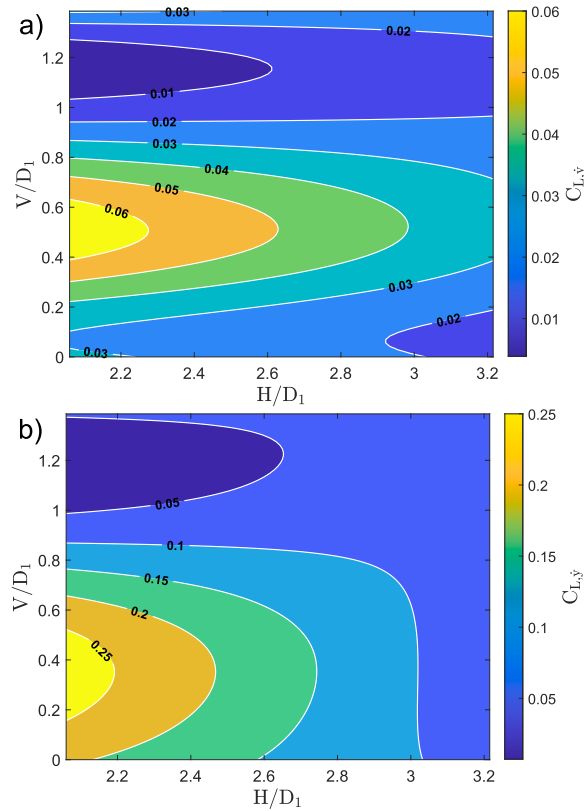
Fig. 11. Variations of the lift coefficient in phase with cylinder velocity in the transverse direction ($C_{L,\dot{y}}$) for different horizontal and vertical offsets. Upstream cylinder (a) and downstream cylinder (b).

The time-averaged power transfer between the fluid and the vibrating cylinder is expressed by the component of the lift force coefficient in phase with transverse velocity of the cylinder, given by

$$C_{L,\dot{y}} = \frac{\sqrt{2}\langle C'_L \dot{y} \rangle}{\sqrt{\langle \dot{y}^2 \rangle}} \tag{22}$$

where $\langle \cdot \rangle$ denotes time averaging, C'_L is the fluctuating part of the lift force coefficient, $\dot{y}$ is the cylinder velocity in the transverse direction. A positive $C_{L,\dot{y}}$ value denotes an exciting effect indicating power transfer from the fluid to the cylinder. A negative $C_{L,\dot{y}}$ value denotes a damping effect. The values of $C_{L,\dot{y}}$ versus L/D_1 and V/D_1 are shown in Fig. 11. Due to the self-excited nature of the cylinders vibration, $C_{L,\dot{y}}$ is positive for both cylinders in all the investigated configurations. The values of $C_{L,\dot{y}}$ are much lower for UC compared with the values of $C_{L,\dot{y}}$ for DC. Comparing contours presented in Figs. 7 and 11, it is apparent that there is an overlap between the high response zones of $A_{Y,max}/D_n$ and the zones with high $C_{L,\dot{y}}$ values.

3.2. Flow patterns

It is well known that the flow around multiple vibrating bodies located in close proximity is very complex. Flow field visualizations are useful to understand the underlying physics of the problem. Fig. 12 shows the instantaneous vorticity contours for selected representative configurations.

For the ($L/D_1 = 2.06$, $V/D_1 = 0$) configuration shown in Fig. 12a, the shear layers developed from UC are reattaching on DC in a quasi-static manner. The result of shear layers reattachment is the formation of a single von Kàrmàn vortex street in the wake. The shedding pattern in this case can be classified as a 2S type mode, characterized by two single vortices developed per shedding cycle. With the increasing V/D_1, the flow in the gap between the cylinders becomes asymmetric. For $L/D_1 = 2.06$ and $V/D_1 = (0.23 - 0.92)$, the shear layers reattachment is intermittent (Fig. 12c and e), depending on the transverse position of DC. When DC is translating close to its maximum transverse displacement away from the UC centerline, the gap flow biased towards the wake of UC is present (Fig. 12c). When DC is translating close to the UC centerline the reattachment occurs. Further increase in V/D_1 (i.e. $V/D_1 = 1.39$) results in the formation of two separate vortex streets behind each of the cylinders (Fig. 12g).

For $L/D_1 = 3.22$ and $V/D_1 = (0 - 0.46)$ (Fig. 12b and d) the vortices from UC roll up in the gap between the cylinders and are impinging on the surface of DC. A single vortex street is formed in the near wake of the cylinders and shedding mode is 2S type. When
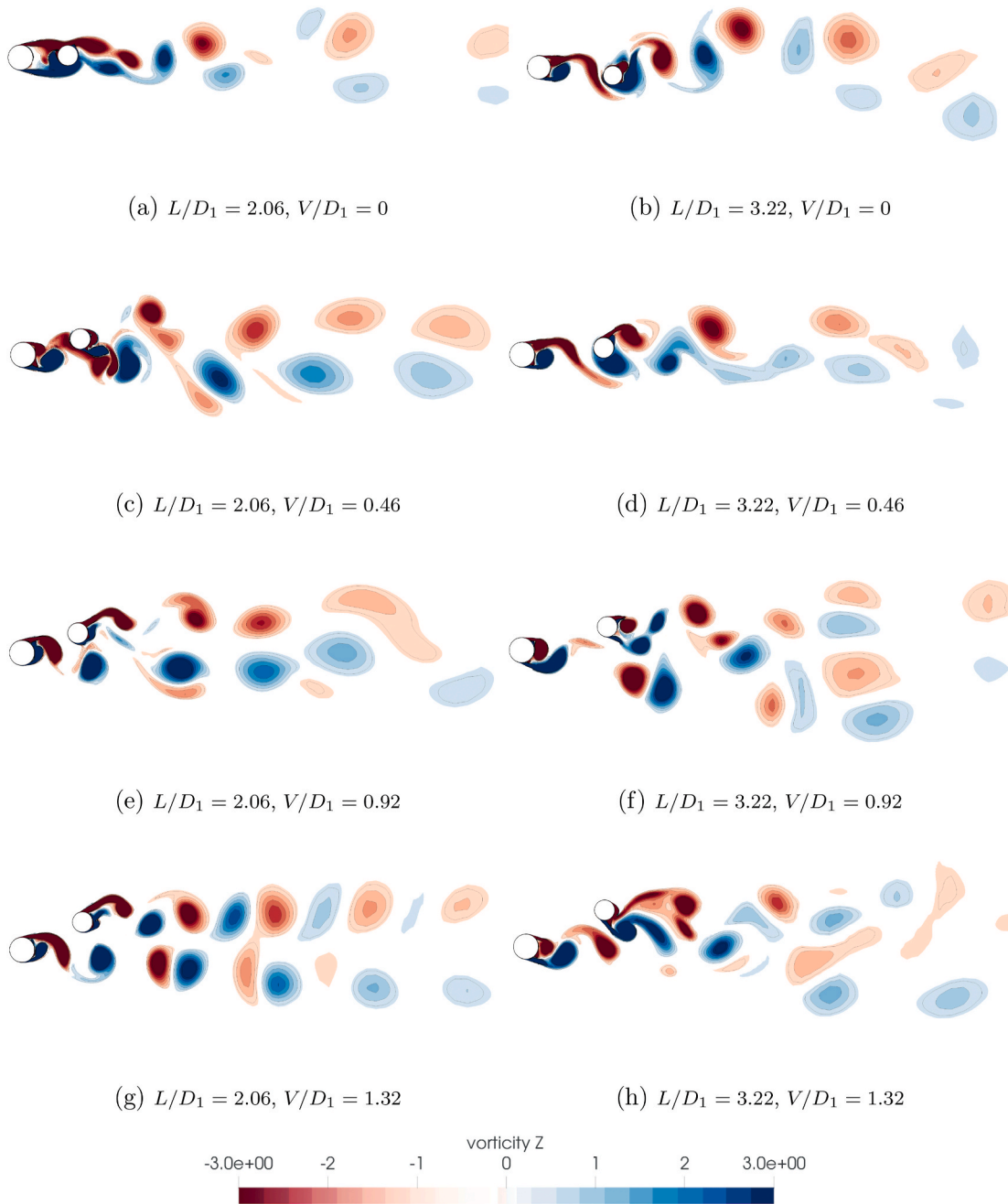
(a) $L/D_1 = 2.06$, $V/D_1 = 0$

(b) $L/D_1 = 3.22$, $V/D_1 = 0$

(c) $L/D_1 = 2.06$, $V/D_1 = 0.46$

(d) $L/D_1 = 3.22$, $V/D_1 = 0.46$

(e) $L/D_1 = 2.06$, $V/D_1 = 0.92$

(f) $L/D_1 = 3.22$, $V/D_1 = 0.92$

(g) $L/D_1 = 2.06$, $V/D_1 = 1.32$

(h) $L/D_1 = 3.22$, $V/D_1 = 1.32$

Fig. 12. Instantaneous vorticity fields for the fully developed flow around the investigated configurations.

the V/D_1 is large, i.e. $V/D_1 = (0.92 - 1.39)$, two irregular vortex streets are formed, see Fig. 12f and h. In those configurations, the shedding mode of UC is 2S type and the shedding mode of DC is 2P (two pairs shed per cycle) type. However, due to the interaction of the inner shear layers, the vortices with opposing direction of rotation are canceling out each other. The wake becomes asymmetric and the vortex street behind the cylinders appears irregular.

3.3. Spectral analysis of responses and orbital trajectories

A Fast Fourier Transform (FFT) is used to analyze the frequency of the transverse vibration displacements (Y_n/D_n) and $C_{L,n}$ for the investigated configurations of two cylinders. The frequencies in power spectral density (PSD) plots are normalized by the fundamental natural frequencies in transverse direction (f_{ny}) of UC and DC, accordingly. In order to investigate cylinders behavior when no flow
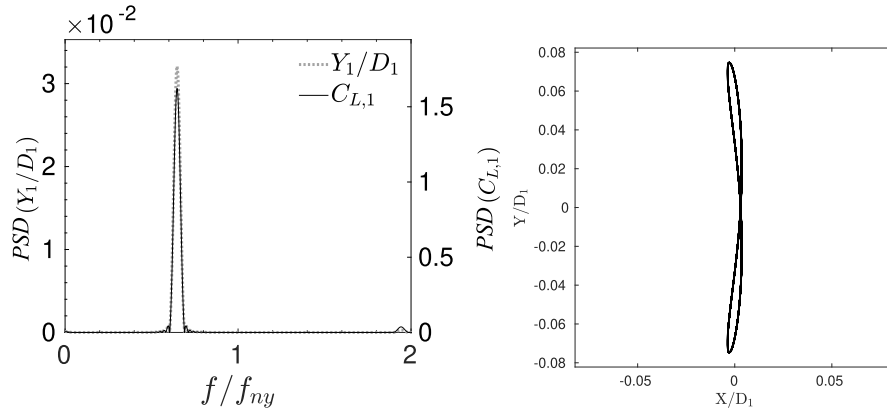
(a) Upstream cylinder
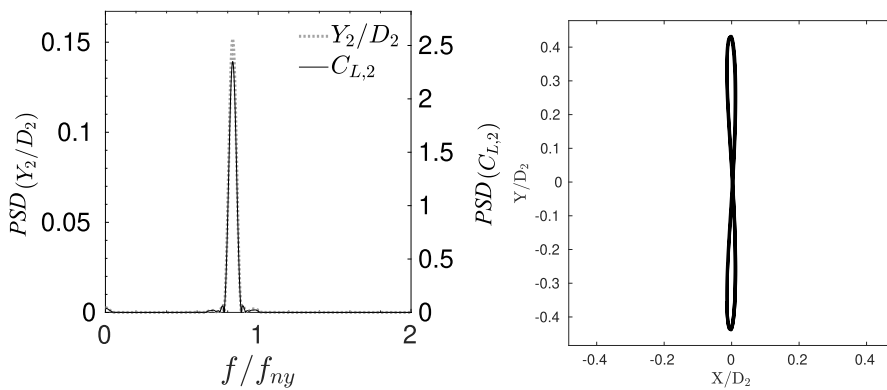
(b) Downstream cylinder

Fig. 13. Power spectral densities of transverse displacement and lift coefficient for single isolated cylinder configurations.

interference effects are present, additional simulations for the cases of isolated cylinder configuration are performed. The cylinder properties in isolated configurations correspond to the properties of UC and DC listed in Table 1. The $PSD_{(Y_n/D_n)}$, $PSD_{(C_{L,n})}$ and motion trajectories for the isolated cylinder cases are shown in Fig. 13. The trajectories in the isolated configuration are typical 'figure eight' patterns as shown in Fig. 13a and b. The transverse vibration frequency of UC is significantly lower than its transverse natural frequency (Fig. 13a) and consequently the vibration amplitudes are small. Fig. 13b shows the $PSD_{(Y_2/D_2)}$ and for DC. A single peak in the $PSD_{(Y_2/D_2)}$ curve is observed at a frequency slightly lower than f_{ny}. This indicates that the cylinder is at the onset of the lock-in. At low mass ratios, the natural frequency in still water is less than the structural natural frequency. Therefore, the lock-in frequency is generally smaller than $f/fny = 1$. The lock-in condition can be observed in the trajectory plot of DC (Fig. 13b) where the Y_2/D_2 amplitude is large compared to the amplitude of Y_1/D_1 of UC (Fig. 13a). The $PSD_{(Y_n/D_n)}$ and $PSD_{(C_{L,n})}$ plots for the selected representative cases of two cylinders in proximity are presented in Fig. 14. A clear difference compared to the isolated cylinder spectra is the appearance of additional harmonics in Y_n/D_n and $C_{L,n}$ signals, and in some cases, broad-banded character of the $PSD_{(Y_n/D_n)}$ and $PSD_{(C_{L,n})}$. In the $(L/D_1 = 2.06, V/D_1 = 0)$ configuration, the peak frequency in $PSD_{(Y_n/D_n)}$ is shifted to slightly higher frequency (Fig. 14a) compared to that of the isolated cylinder case (Fig. 13). The vibration frequency of DC deviates from the Strouhal law and is close to the frequency of vortex shedding from UC. When the $PSD_{(C_{L,n})}$ of both UC and DC are plotted in the same figure (Fig. 15) and normalized by the f_{ny} of DC, it is evident that both cylinders vibrate with the same frequency. This is consequent with the observations made in the near wake analysis where the shear layer reattachment is persistent in this configuration (Fig. 12a).

For the $(L/D_1 = 2.06, V/D_1 = 0.46)$ configuration, in which DC experiences peak in-line and transverse vibration amplitudes the $PSD_{(Y_2/D_2)}$ and $PSD_{(C_{L,2})}$ are broad-banded, see Fig. 14c. The cause of broad-banded character of the $PSD_{(C_{L,2})}$ is the interaction of the shear layers from DC with the shear layers from UC and disturbances in the gap between the cylinders. Fig. 14c shows that there are two dominant peaks in the $PSD_{(C_{L,2})}$ plot, i.e. one peak located close to the natural frequency of the cylinder and a second peak at
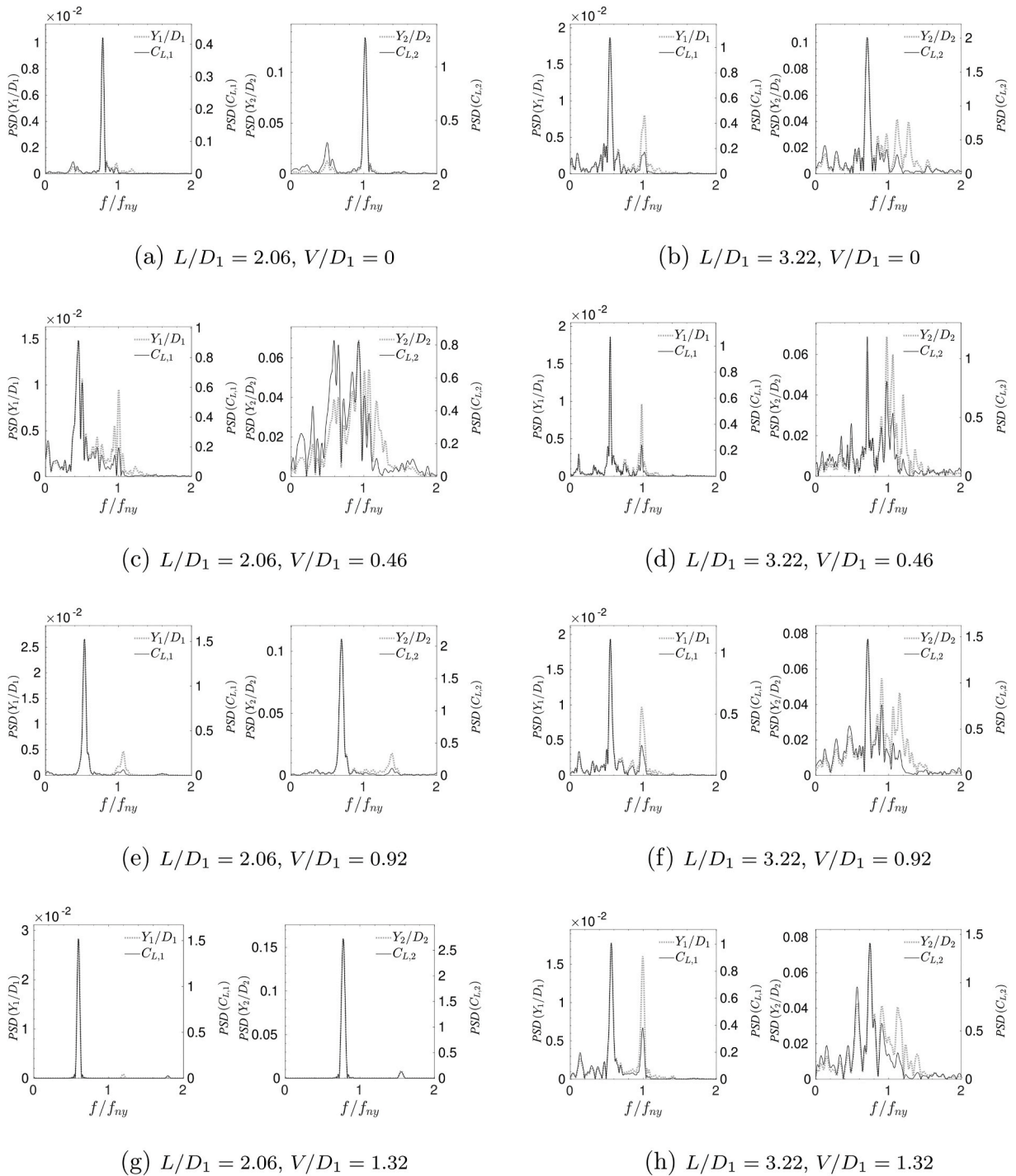
(a) $L/D_1 = 2.06, V/D_1 = 0$ (b) $L/D_1 = 3.22, V/D_1 = 0$

(c) $L/D_1 = 2.06, V/D_1 = 0.46$ (d) $L/D_1 = 3.22, V/D_1 = 0.46$

(e) $L/D_1 = 2.06, V/D_1 = 0.92$ (f) $L/D_1 = 3.22, V/D_1 = 0.92$

(g) $L/D_1 = 2.06, V/D_1 = 1.32$ (h) $L/D_1 = 3.22, V/D_1 = 1.32$

Fig. 14. Power spectral densities of transverse displacement and lift coefficient for two-cylinder configurations.

approximately half the natural frequency. At $V/D_1 = 0.46$, DC is interacting only with the top shear layer from UC, hence the hydrodynamic forcing has a frequency equal to half the vortex shedding frequency of UC.

The $PSD_{(Y_n/D_n)}$ and $PSD_{(C_{L,n})}$ for the ($L/D_1 = 2.06, V/D_1 = 0.92$) and ($L/D_1 = 2.06, V/D_1 = 1.32$) configurations (see Fig. 14e and g) have only one dominant peak in the spectra and the peak frequencies are close to those observed for the isolated cylinder cases. This indicates that no significant wake interference effect occurs in these two configurations. For larger L/D_1, Fig. 14b, d, 14f, and 14h show many peaks in the $PSD_{(Y_2/D_2)}$ and $PSD_{(C_{L,2})}$ curves. This indicates that the wake interference effects are significant for the vibration
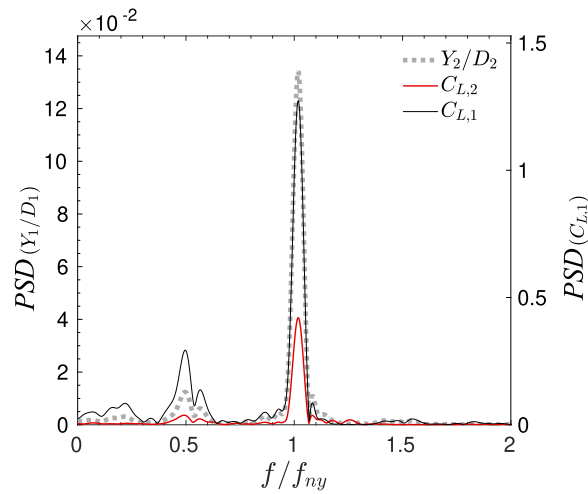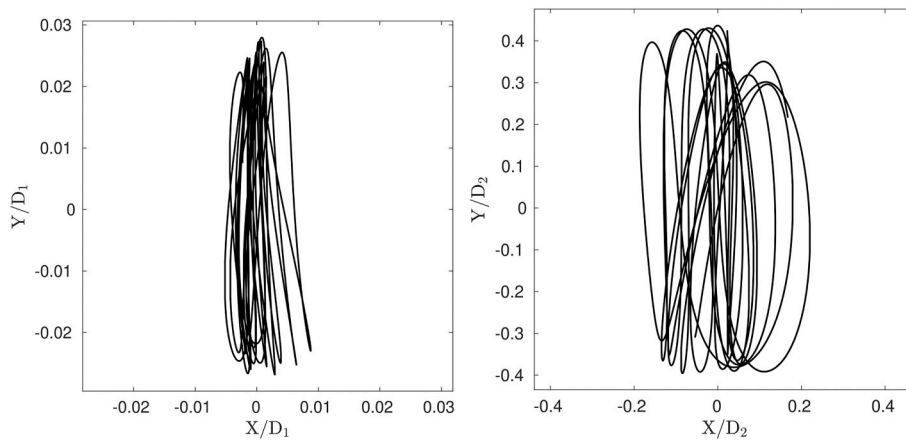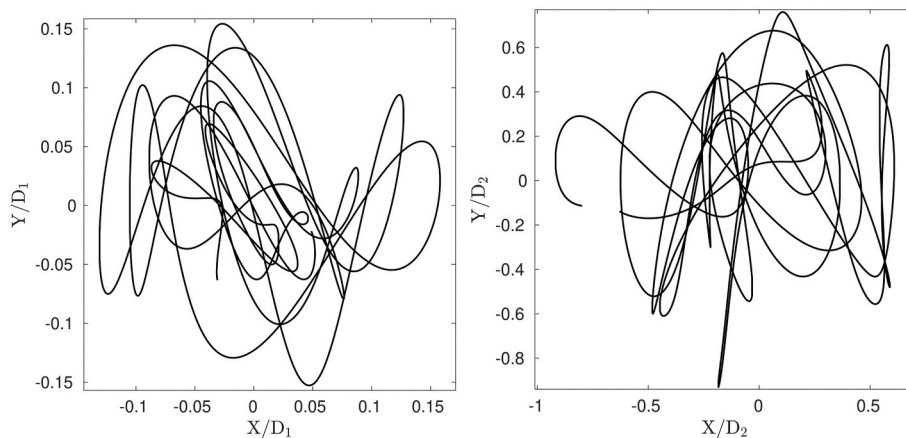
Fig. 15. Power spectral densities of transverse displacement and lift coefficient for $L/D_1 = 2.06$, $V/D_1 = 0$ configuration.

(a) $L/D_1 = 2.06$, $V/D_1 = 0$

(b) $L/D_1 = 2.06$, $V/D_1 = 0.46$

Fig. 16. Motion trajectories of UC (left) and DC (right) for different horizontal and vertical offsets.
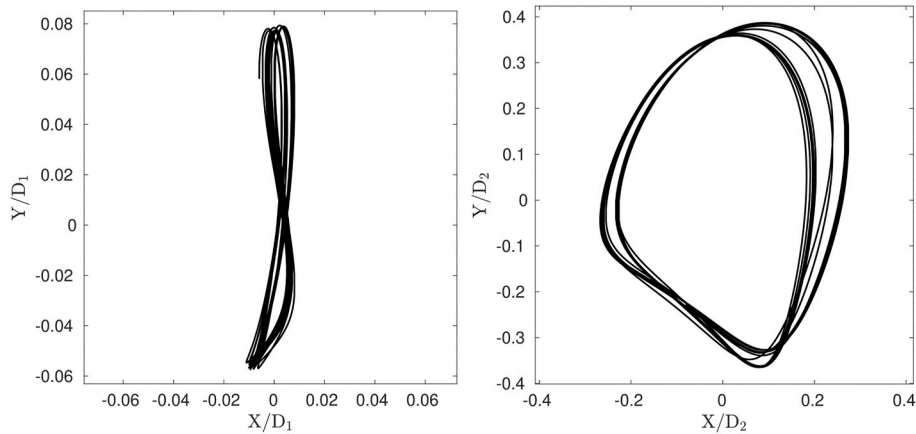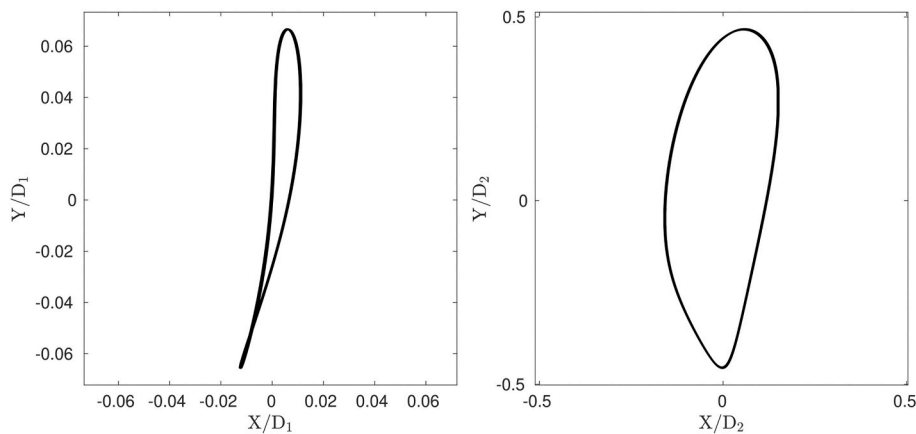
(c) $L/D_1 = 2.06$, $V/D_1 = 0.92$

(d) $L/D_1 = 2.06$, $V/D_1 = 1.32$

Fig. 16. (*continued*).

response of DC even at large V/D_1. The $PSD_{(Y_1/D_1)}$ and $PSD_{(C_{L,1})}$ curves have one dominant peak and the respective peak frequencies are close to those observed in the corresponding spectra for the isolated UC cylinder case.

The motion trajectory plots are shown in Figs. 16 and 17. They reveal that the trajectory of UC has the classic 'figure eight' shape in configurations where the proximity effects are not significant (Fig. 16a, c, 16d, 17d). For the configurations ($L/D_1 = 2.06$, $V/D_1 = 0.46$), ($L/D_1 = 3.22$, $V/D_1 = 0.46$), and ($L/D_1 = 3.22$, $V/D_1 = 0.92$) the trajectories become irregular. For the cases with $L/D_1 = 2.06$, the DC trajectory is oval and regular (Fig. 16a, c, 16d) except for $V/D_1 = 0.23$ and $V/D_1 = 0.46$ where it becomes irregular (Fig. 16b). For the cases with $L/D_1 = 3.22$, the DC trajectory is irregular (Fig. 17). The irregularity in the motion trajectories is correlated with the response zones identified in Section 3.1. Generally, in the high-response zone where the wake-induced vibrations are dominating, the trajectories appear to be irregular and A_X/D_2 is increased significantly compared to the cases where the wake interference effects are small.

4. Conclusions

Wake-induced vibrations of two cylinders with different diameters arranged with different horizontal offset $L/D_1 = [2.06, 3.22]$ and vertical offset $V/D_1 = [0, 0.23, 0.46, 0.92, 1.39]$ have been investigated numerically. The 2D computational model has been set up to simulate the fluid-structure interaction of two subsea flowlines laid over close to each other. The structural parameters have been provided by a detailed finite element model of the flowline sections in the vicinity of the free span.

The simulations have been performed at subcritical Reynolds numbers using URANS approach for turbulence modeling. The results for the flow around two cylinders vibrating with two degrees-of-freedom have been presented. Vibration amplitude response and force coefficients have been presented with respect to the horizontal and vertical position of the downstream cylinder. Three distinct zones
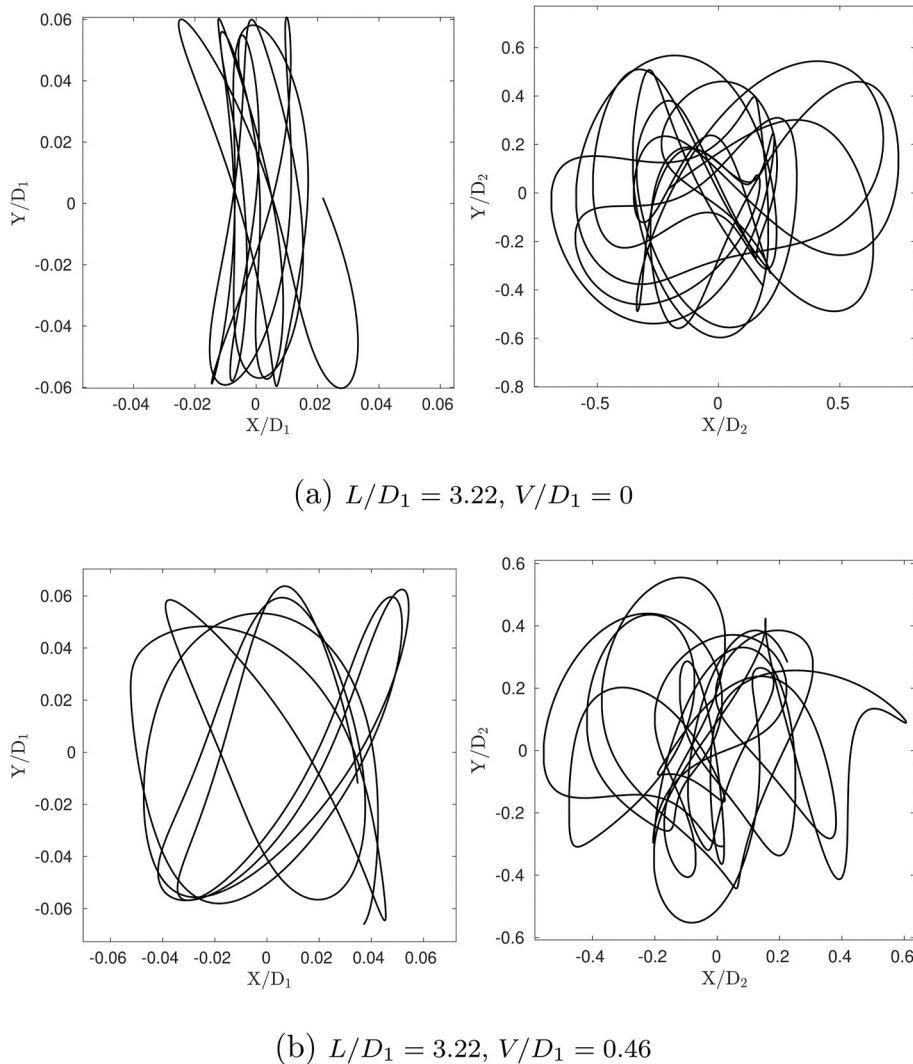
(a) $L/D_1 = 3.22$, $V/D_1 = 0$

(b) $L/D_1 = 3.22$, $V/D_1 = 0.46$

Fig. 17. Motion trajectories of UC (left) and DC (right) for different horizontal and vertical offsets.

have been identified based on the vibration responses of the cylinders observed for the investigated configurations. The oscillation regimes have been characterized based on the vibration amplitudes, flow field analysis of the cylinders near wake, and frequency domain analysis of the recorded displacements and forces time series.

A series of numerical tests has been performed in order to validate the model by comparing with the available experimental data. It appears that the present model predicts the drag reduction in tandem cylinders configurations reasonably well. Furthermore, the present model has been validated against the experimental data for the single cylinder vibrating with 2DOF in the subcritical Reynolds number regime. The model provides reasonable accuracy with respect to prediction of the vibration amplitudes and frequencies.

Based on the effect of V/D_1 on $A_{Y,max}/D_n$, three distinct zones can be distinguished: (i) low-response zone close to UC centerline, (ii) high-response zone at intermediate vertical offsets ($V/D_1 = 0.2 - 0.6$), and (iii) low-response zone at large vertical offsets ($V/D_1 > 0.6$). The peak response in $A_{Y,max}/D_n$ is observed for ($L/D_1 = 2.06$, $V/D_1 = 0.46$) configuration. When L/D_1 is increased from 2.06 to 3.22, $A_{Y,max}/D_n$ is considerably less sensitive to change in V/D_1.

Compared with the response of an isolated cylinder, the in-line vibration amplitudes of a cylinder subject to wake-induced vibrations in the high-response zone are increased significantly. The peak amplitude of the in-line vibration is similar in magnitude to the transverse vibration amplitude. The wake induced effects decay rapidly with an increase in the horizontal offset between the cylinders.

Based on the findings of the present study, a list of recommendations for future work has been formulated:

- Investigation of additional configurations, with emphasis on very small separation cases ($L/D_1 < 2.06$).
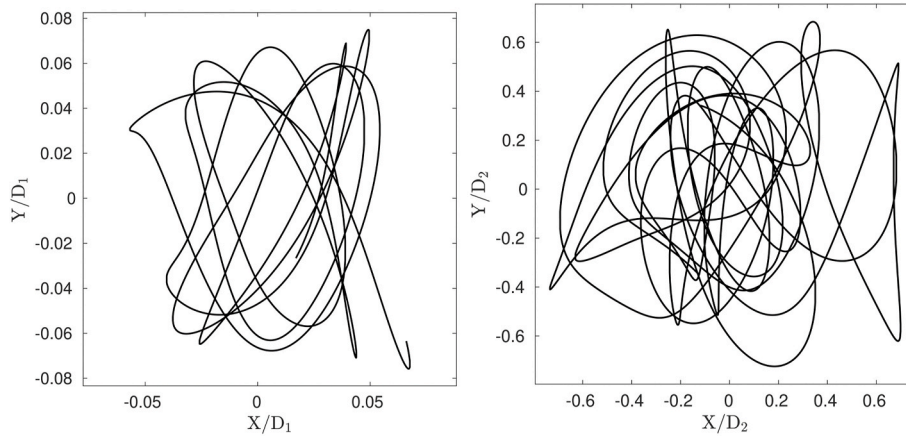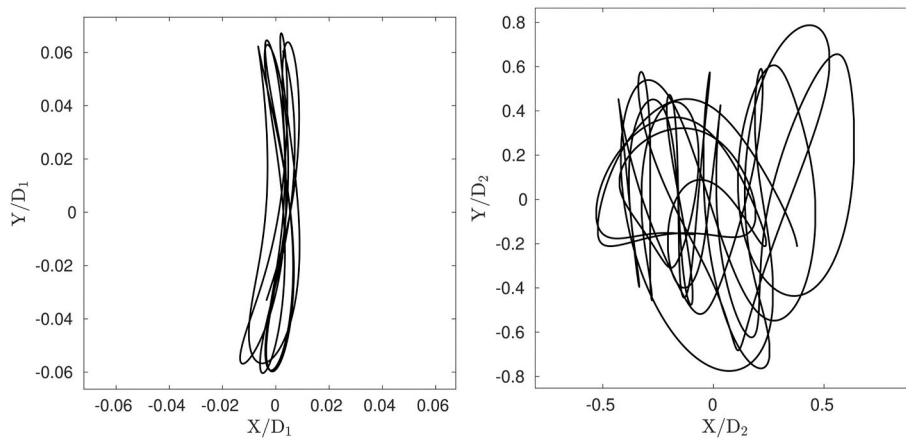
(c) $L/D_1 = 3.22$, $V/D_1 = 0.92$

(d) $L/D_1 = 3.22$, $V/D_1 = 1.32$

Fig. 17. (*continued*).

- Investigation of higher Reynolds number cases. In particular, a comparison between coefficients obtained for the subcritical, critical and transcritical regimes would be of practical interest.
- The dynamic response of free spanning pipelines is expected to be influenced by the bottom boundary layer profile. It is, therefore, desirable to further investigate the importance of those effects on global response of the system, using for example 3D CFD model for FSI simulations.

Declaration of competing interest

The authors declare that they have no known competing financial interests or personal relationships that could have appeared to influence the work reported in this paper.

Acknowledgments

References

[1] Dnv GL. DNVGL-RP-F203, riser interference. Norway: Høvik; 2007.

[2] Lyngsaunet OD, Nystrøm PR, Endal G, Levold E, Stokholm H. Optimising the Johan Castberg trawl interference design using close lay of rigid flowlines and structural reliability analysis. In: Proceedings of international ocean and polar engineering conference; June 2019. p. 1720–7. Honolulu, Hawaii, USA.

[3] Drago M, Mattioli M, Bruschi R, Vitali L. Insights on the design of free-spanning pipelines. Phil Trans Math Phys Eng Sci 2015;373(2033):1–27.

[4] Bearman P, Zdravkovich M. Flow around a circular cylinder near a plane boundary. J Fluid Mech 1978;89:33–47.

[5] Wang XK, Hao Z, Tan SK. Vortex-induced vibrations of a neutrally buoyant circular cylinder near a plane wall. J Fluid Struct 2013;39(Supplement C):188–204.

[6] Williamson CHK, Govardhan R. Vortex-induced vibrations. Annu Rev Fluid Mech 2004;36(1):413–55.

[7] Sarpkaya T. A critical review of the intrinsic nature of vortex-induced vibrations. J Fluid Struct 2004;19(4):389–447.

[8] Gabbai RD, Benaroya H. An overview of modeling and experiments of vortex-induced vibration of circular cylinders. J Sound Vib 2005;282:575–616.

[9] Bearman PW. Circular cylinder wakes and vortex-induced vibrations. J Fluid Struct 2011;27(5):648–58.

[10] Zdravkovich MM. Flow around circular cylinders: volume I: fundamentals. Oxford University Press; 1997.

[11] Sumner D. Two circular cylinders in cross-flow: a review. J Fluid Struct 2010;26(6):849–99.

[12] Zdravkovich MM. Classification of flow-induced oscillations of two parallel circular cylinder in various arrangements. ASME Winter Annual Meeting, Symposium on Flow-Induced Vibrations 1984;2(1 – 18).

[13] Zdravkovich MM. Review of interference-induced oscillations in flow past two parallel circular cylinders in various arrangement. J Wind Eng Ind Aerod 1988; 28:183–200.

[14] Medeiros EB, Zdravkovich MM. Interference-induced oscillations of two unequal cylinders. J Wind Eng Ind Aerod 1992;41(1):753–62.

[15] Mahbub Alam Md, Moriya M, Takai K, Sakamoto H. Fluctuating fluid forces acting on two circular cylinders in a tandem arrangement at a subcritical Reynolds number. J Wind Eng Ind Aerod 2003;91(1):139–54.

[16] Mahbub Alam Md, Moriya M, Takai K, Sakamoto H. Effect of a t-shaped plate on reduction in fluid forces on two tandem cylinders in a cross-flow. J Wind Eng Ind Aerod 2006;94(1):525–51.

[17] Zdravkovich MM. Review of flow interference between two circular cylinders in various arrangements. J Fluid Eng 1977;99(4):618–33.

[18] Bokaian A, Geoola F. Wake-induced galloping of two interfering circular cylinders. J Fluid Mech 1984;146:384–415.

[19] King R, Jones DJ. Wake interaction experiments with two flexible circular cylinders in flowing water. J Sound Vib 1984;45(2):259–89.

[20] Brika D, Laneville A. The flow interaction between a stationary cylinder and a downstream flexible cylinder. J Fluid Struct 1999;13(5):579–606.

[21] Assi GRS, Bearman PW, Meneghini JR. On the wake-induced vibration of tandem circular cylinders: the vortex interaction excitation mechanism. J Fluid Mech 2010;661. 365â€"401.

[22] Ong MC, Utnes T, Holmedal LE, Myrhaug D, Pettersen B. Numerical simulation of flow around a circular cylinder close to a flat seabed at high Reynolds numbers using a k - ε model. Coast Eng 2010;57(10):931–47.

[23] Han Xiangxi, Lin Wei, Wang Dongjiao, Qiu Ang, Feng Zhiqiang, Tang Youhong, Wu Jiaming. Numerical simulation of super upper branch of a cylindrical structure with a low mass ratio. Ocean Eng 2018;168:108–20.

[24] Kang Zhuang, Ni Wen-chi, Zhang Xu, Sun Li-ping. Two improvements on numerical simulation of 2-dof vortex-induced vibration with low mass ratio. China Ocean Eng Dec 2017;31(6):764–72.

[25] Jauvtis N, Williamson CHK. The effect of two degrees of freedom on vortex-induced vibration at low mass and damping. J Fluid Mech 2004;509:23–62.

[26] Kinaci OK. 2-D URANS simulations of vortex induced vibrations of circular cylinder at Trsl3 flow regime. J Appl Fluid Mech 2016;9(5):2537–44.

[27] Menter FR, Kuntz M, Langtry R. Ten years of industrial experience with the SST turbulence model. Heat Mass Tran 2003;4:625–32.

[28] Hoerner SF. Fluid-Dynamic Drag: practical information on aerodynamic drag and hydrodynamic resistance. 1958. p. 137.

[29] Blevins RD, Coughran CS. Experimental investigation of vortex-induced vibration in one and two dimensions with variable mass, damping, and Reynolds number. J Fluid Eng 2009;131(10). 101202 – 101202–7.

[30] Dnv GL. DNVGL-RP-C205, environmental conditions and environmental loads. Norway: Høvik; 2010.